

See discussions, stats, and author profiles for this publication at: <https://www.researchgate.net/publication/41197760>

# Effect of Humidity on Nanoscale Adhesion on Self-Assembled Thiol Monolayers Studied by Dynamic Force Spectroscopy

## ARTICLE

Source: OAI

### CITATIONS

4

### READS

13

## 4 AUTHORS, INCLUDING:



[Hubert Gojzewski](#)

University of Twente

**30** PUBLICATIONS **129** CITATIONS

[SEE PROFILE](#)



[Michael Kappl](#)

Max Planck Institute for Polymer Research

**143** PUBLICATIONS **3,913** CITATIONS

[SEE PROFILE](#)



[Arkadiusz Ptak](#)

Poznan University of Technology

**34** PUBLICATIONS **416** CITATIONS

[SEE PROFILE](#)

## Effect of Humidity on Nanoscale Adhesion on Self-Assembled Thiol Monolayers Studied by Dynamic Force Spectroscopy

Hubert Gojzewski,<sup>†,‡</sup> Michael Kappl,<sup>‡</sup> Arkadiusz Ptak,<sup>†</sup> and Hans-Jürgen Butt<sup>\*,‡</sup>

<sup>†</sup>*Institute of Physics, Poznan University of Technology, Nieszawska 13A, PL-60965 Poznan, Poland, and*

<sup>‡</sup>*Max Planck Institute for Polymer Research, Ackermannweg 10, D-55128 Mainz, Germany*

Received July 14, 2009. Revised Manuscript Received September 5, 2009

The adhesion force between silicon nitride tips of an atomic force microscope and different self-assembled thiol monolayers (SAMs) was measured at different loading rates and humidity. SAMs were formed from HS(CH<sub>2</sub>)<sub>n</sub>CH<sub>3</sub> with  $n = 6, 8, 9, 10, 15$  and HS(CH<sub>2</sub>)<sub>n</sub>OH with  $n = 6, 9, 11, 16$ . With a special setup, the loading rate could be increased to  $10^7$  nN s<sup>-1</sup>. For the interaction with two-dimensional crystalline CH<sub>3</sub>-terminated SAMs ( $n \geq 8$ ), two regimes can be distinguished. At loading rates below  $10^4$ – $10^5$  nN s<sup>-1</sup>, the adhesion force increased proportional to the logarithm of the loading rate. Adhesion is most likely dominated by van der Waals attraction. At higher loading rates, the adhesion forces increased steeper with the logarithm of the loading rate. The specific process limiting separation is not yet identified. On OH-terminated SAMs, the adhesion force was ~6 times higher than on the CH<sub>3</sub>-terminated SAMs, even at low humidity. This can partially, but not fully, be explained by hydrogen bridges forming between the hydroxyl groups of the monolayer and silanol groups of the tip. For relative humidity above 10%, the capillary force further increased the adhesion force, which reached a maximum at values of relative humidity between 40% and 80%. Adhesion force versus loading rate ( $F_{ad}$  versus  $r_F$ ) curves increased roughly linearly over the whole range of loading rates. The slope depended on the humidity, and it is correlated with the absolute strength of the capillary force.

### Introduction

Adhesion between solid surfaces is of importance in many industrial applications and biological phenomena, and for fundamental science.<sup>1</sup> Recently, nanoadhesion, that is, the adhesion of nanometer sized contacts,<sup>2</sup> has become a topic of interest. It was shown that the sticking properties can be much improved,<sup>3</sup> for instance, by mimicking adhesion systems of animals that create adhesive nanocontacts between their soft feet tissue and various types of surfaces.<sup>4</sup> For this reason, soft matter surfaces such as polymers and proteins, and systems such as self-assembled monolayers are promising candidates for applications. For such materials, the adhesion can be controlled by temperature,<sup>5</sup> vapor environment,<sup>6</sup> surface separation rates,<sup>7,8</sup> and contact geometry.<sup>9</sup>

Nowadays, the atomic force microscope<sup>10</sup> (AFM) is the most prevalent technique for studying adhesion at the nanoscale.<sup>11</sup> In the so-called dynamic force spectroscopy AFM mode, adhesion is measured as a function of separation rates (separation velocities) between the AFM tip and sample.<sup>7,8</sup> This not only allows one to obtain static information, but also the dynamics of the rupture process is probed.<sup>12,13</sup>

Dynamic force spectroscopy was introduced over one decade ago by Evans and Ritchie.<sup>13</sup> They have shown that studying the effect of force on dissociation kinetics of molecular interactions can provide information on chemical bonds. According to their theory, the adhesion force mediated by single bonds increases linearly with the logarithm of the separation rate. This logarithmic dependence is often difficult to verify, since in commercial AFMs the range of separation rates is limited to typically  $100 \mu\text{m s}^{-1}$ . For this reason, we modified an AFM as described by Ptak et al.<sup>7</sup> to extend the range of accessible separation rates by up to 4 orders of magnitude and to be able to measure at adjustable humidity.

As a model system, we studied well-known and characterized self-assembled thiol monolayers (SAMs).<sup>14–22</sup> They form stable and densely packed two-dimensional crystal structures on a substrate of Au(111). Thiol monolayers are stabilized by the strong binding energy of the sulfur–gold bond of approximately  $184 \text{ kJ mol}^{-1}$ .<sup>15</sup> Alkanethiols and their analogues with a functional group are further stabilized by van der Waals interactions between the alkyl chains. Their surface properties as well as their thickness can be varied by using different end groups (e.g., CH<sub>3</sub>, OH, NH<sub>2</sub>, COOH, CF<sub>3</sub>) and by the number of CH<sub>2</sub> groups in the chain, respectively.

\*Corresponding author. E-mail: butt@mpip-mainz.mpg.de. Telephone: 0049-6131-379 111. Fax: 0049-6131-379 310.

(1) Packham, D. E. *Handbook of Adhesion*, 2nd ed.; John Wiley & Sons: Chichester, West Sussex, 2005.

(2) Persson, B. N. J. *Wear* **2003**, 254, 832–834.

(3) Lee, H.; Lee, B. P.; Messersmith, P. B. *Nature* **2007**, 448, 338–U4.

(4) Autumn, K.; Liang, Y. A.; Hsieh, S. T.; Zesch, W.; Chan, W. P.; Kenny, T. W.; Fearing, R.; Full, R. J. *Nature* **2000**, 405, 681–685.

(5) Kim, K. S.; Ando, Y.; Kim, K. W. *Nanotechnology* **2008**, 19, 105701.

(6) Xiao, X. D.; Qian, L. M. *Langmuir* **2000**, 16, 8153–8158.

(7) Ptak, A.; Kappl, M.; Butt, H. J. *Appl. Phys. Lett.* **2006**, 88, 263109.

(8) Ptak, A.; Kappl, M.; Moreno-Flores, S.; Gojzewski, H.; Butt, H. J. *Langmuir* **2009**, 25, 256–261.

(9) Shull, K. R. *Mater. Sci. Eng., R* **2002**, 36, 1–45.

(10) Binnig, G.; Quate, C. F.; Gerber, C. *Phys. Rev. Lett.* **1986**, 56, 930–933.

(11) Drelich, J.; Mittal, K. L. *Atomic Force Microscopy in Adhesion Studies*; Brill Academic Publishers: Boston, 2005.

(12) Bell, G. I. *Science* **1978**, 200, 618–627.

(13) Evans, E.; Ritchie, K. *Biophys. J.* **1997**, 72, 1541–1555.

(14) Evans, S. D.; Sharma, R.; Ulman, A. *Langmuir* **1991**, 7, 156–161.

(15) Lio, A.; Morant, C.; Ogletree, D. F.; Salmeron, M. *J. Phys. Chem. B* **1997**, 101, 4767–4773.

(16) Azzam, W.; Cyganik, P.; Witte, G.; Buck, M.; Woll, C. *Langmuir* **2003**, 19, 8262–8270.

(17) Liu, Y. F.; Yang, Y. C.; Lee, Y. L. *Nanotechnology* **2008**, 19, 065609.

(18) Yang, Y. C.; Chang, T. Y.; Lee, Y. L. *J. Phys. Chem. C* **2007**, 111, 4014–4020.

(19) Bain, C. D.; Troughton, E. B.; Tao, Y. T.; Evall, J.; Whitesides, G. M.; Nuzzo, R. G. *J. Am. Chem. Soc.* **1989**, 111, 321–335.

(20) Wenzl, I.; Yam, C. M.; Barriet, D.; Lee, T. R. *Langmuir* **2003**, 19, 10217–10224.

(21) Barrena, E.; Ocal, C.; Salmeron, M. *J. Chem. Phys.* **2000**, 113, 2413–2418.

(22) Subramanian, S.; Sampath, S. *Pramana* **2005**, 65, 753–761.

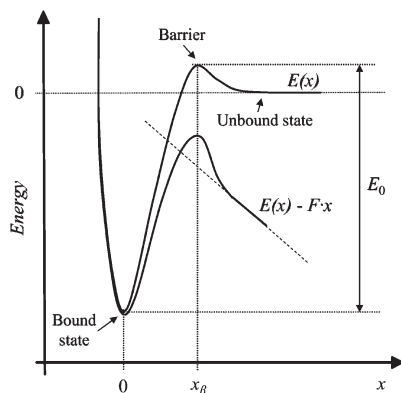


**Figure 1.** Schematic of the interaction potential of a bond with an activation barrier. The external force  $F$  tilts the potential and lowers the activation barrier  $E_0$ .

In the presence of a vapor, adhesion on lyophilic surfaces is often dominated by a liquid bridge formed by capillary condensation. The liquid bridge leads to an attractive capillary force.<sup>23</sup> The most important vapor is water, since it is practically always present. The capillary forces occur on hydrophilic surfaces and give rise to significant adhesion forces, being significantly stronger than those in dry air.<sup>24</sup> Mostly, the adhesion as a function of humidity initially increases to reach a maximum and then decreases again.<sup>6</sup>

Since adhesion is a complex function of separation rate and humidity, in this paper we describe results of adhesion experiments between AFM tips and SAMs for different separation rates (loading rates) and different humidity. SAMs of two types of molecules,  $\text{CH}_3$ - and  $\text{OH}$ -terminated thiols leading to hydrophobic and hydrophilic surfaces, were studied. Measurements over many orders of magnitude of separation rates are performed to obtain significant data describing adhesion phenomena in more detail.

## Theory

For a quantitative interpretation of dynamic force spectroscopy, a physical model is required. We apply the model of Evans and Ritchie<sup>13</sup> to calculate the kinetic parameters describing an adhesive bond. Their theoretical explanation of the separation rate for a single chemical bond is given based on the Bell model<sup>12</sup> and is known as the Bell–Evans model. An unbinding process is modeled as the escape from a potential well under the influence of the external loading force. This external load tilts the “energy landscape” of the interaction potential, facilitating the thermally activated escape from the bound state (Figure 1).

To describe bond rupture, the probability  $P(t)$  of being in the bound state at the time  $t$  is defined.  $P(t)$  decreases with time due to dissociation. Dissociation is described by a dissociation rate constant  $k_{\text{off}}$  (also called kinetic off-rate) that is based on a term introduced by Bell that describes the reduction of the activation barrier under the presence of applied loading force  $F(t)$ :

$$k_{\text{off}} = \frac{1}{\tau_D} \exp\left(-\frac{E_0 - F(t) x_\beta}{k_B T}\right) \quad (1)$$

Here,  $E_0$  is the height of the activation energy barrier and  $x_\beta$  is the distance between the bound state and the transition state along

the direction of the external pulling force. We call it activation length.  $\tau_D$  is a characteristic diffusion time of motion in the system,  $k_B$  is the Boltzmann constant, and  $T$  is the temperature. The escape from the bound state  $dP/dt$  due to an applied loading force is given by

$$\frac{dP(t)}{dt} = -k_{\text{off}}(F) P(t) \quad (2)$$

In a typical AFM experiment, the applied force increases linearly with time:

$$F(t) = r_F t \quad (3)$$

where  $r_F$  is the loading rate in  $\text{N s}^{-1}$ . Solving eq 2 leads to  $P(t)$  and later to a most probable unbinding force:

$$F_{\text{ad}} = F_\beta \ln\left(\frac{r_F}{F_\beta k_{\text{off}}^0}\right) \quad (4)$$

Here,  $F_\beta = k_B T/x_\beta$  is the so-called thermal fluctuation force. For a symmetrical distribution of adhesion forces, the value of the most probable unbinding force is equal to the mean adhesion force. Regarding the linear increase of  $F_{\text{ad}}$  with  $\ln r_F$ , eq 4 gives a manner to extract the value of  $x_\beta$  and the thermal dissociation constant  $k_{\text{off}}^0$  (force-free kinetic off-rate), respectively, from the slope and intercept of the  $F_{\text{ad}}$  versus  $\ln r_F$  curve fitted to experimental data. The intercept point is called the thermal loading rate  $r_F^0$ , and it is expressed by

$$r_F^0 = F_\beta k_{\text{off}}^0 \quad (5)$$

The thermal loading rate indicates a “boundary” of the loading rate under which the bond is ruptured only due to thermal fluctuation, since this process is quicker than slow ramping of force. The thermal dissociation constant  $k_{\text{off}}^0$  can be converted to a bond lifetime by  $t_{\text{off}}^0 = 1/k_{\text{off}}^0$ .

## Materials and Methods

**Self-Assembled Monolayers.** SAMs of methyl- ( $\text{CH}_3$ -) and hydroxy- ( $\text{OH}$ -) terminated thiols were formed on Au(111) substrates by immersion in 1 mM thiol in ethanol solution for 12–24 h. The following thiols were used:  $\text{HS}(\text{CH}_2)_n\text{CH}_3$  with  $n = 3^*, 6, 7^*, 8, 9, 10, 11^*, 13^*, 15, 17^*$  and  $\text{HS}(\text{CH}_2)_n\text{OH}$  with  $n = 2^*, 4^*, 6, 9, 11, 16$  (supplier: Alfa-Aesar, Fluka, ProChimia, Sigma-Aldrich; (\*) these thiols were only used for contact angle measurements and scanning tunneling microscopy, and not for adhesion experiments). All thiols were used without further purification (minimal purity is 95%).

**Au(111).** Substrates were prepared by thermal evaporation (Edwards, FL400 model Auto 306, U.K.) of a 80–100 nm thick layer of Au (99.99%, Wieland, Germany) on freshly cleaved mica (Hi-Grade mica, Ted Pella Inc.). The amount of evaporated gold was controlled by using a shutter and a quartz thickness monitor. Mica was preheated at 550 °C for 1 min under a nitrogen stream to avoid contamination preceding the gold evaporation at a base pressure of  $10^{-6}$  to  $2 \times 10^{-6}$  mbar. Furthermore, directly after evaporation, the surfaces were annealed at 600 °C for 2 min under a nitrogen stream and immediately cooled down in ethanol to “freeze” the (111) crystalline structure. After this procedure, an atomically flat Au(111) surface with terraces of 100–200 nm size were obtained. After the time of self-assembly, samples were removed from the thiol solutions, carefully rinsed with ethanol, dried under nitrogen flow for 5–10 min, and directly used for experiments.

(23) Butt, H. J.; Kappl, M. *Adv. Colloid Interface Sci.* **2009**, *146*, 48–60.

(24) Weisenhorn, A. L.; Hansma, P. K.; Albrecht, T. R.; Quate, C. F. *Appl. Phys. Lett.* **1989**, *54*, 2651–2653.

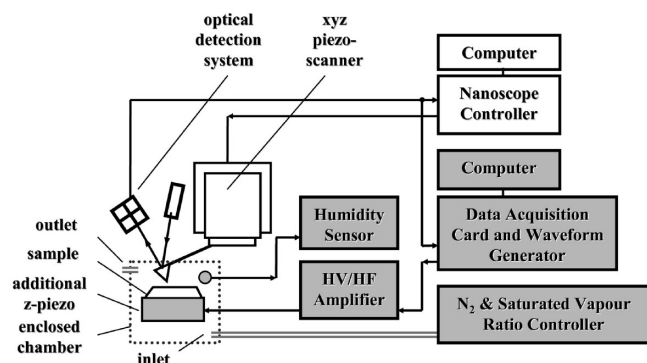


**Figure 2.** Schematic of the modified AFM system. Noncommercial parts which we added are indicated in gray.

**X-ray Diffraction (XRD).** The crystalline structure of substrates (Au(111) on mica) was studied by X-ray diffraction with Cu K $\alpha$  radiation (0.1541 nm) at room temperature using a D8-Advance diffractometer (Bruker Corp.).

**Scanning Tunneling Microscopy.** Scanning tunneling microscope (STM) measurements (Multimode, Veeco Instruments Inc.) were performed in air at room temperature using constant current mode. Typical imaging condition were 0.9 V bias voltage and 10 pA tunnelling current. STM tips were made by mechanically cutting a PtIr (90%/10%, GoodFellow, U.K.) wire. The Au(111) substrates were imaged directly after evaporation and annealing without further treatment. SAM samples were imaged within 1 h after self-assembly (i.e., after removal from the incubation solution).

**Contact Angle Measurements.** The advancing contact angles of CH<sub>3</sub>- and OH-terminated SAMs were measured with a sessile drop setup (DSA-10, Krüss, GmbH, Hamburg, Germany). Droplets of Milli-Q water (18.2 M $\Omega$  cm) of 1–2 mm diameter were deposited on a horizontally placed sample by means of a syringe. The advancing contact angles were measured directly after droplet deposition on both sides of a droplet. The measurements were conducted on a total of 10–15 droplets placed on different locations of a substrate, and the results were averaged. Evans et al.<sup>14</sup> have reported that the contact angle of OH-terminated SAMs can increase (in air) by up to 30° in 30 min after drying. For this reason, we measured the advancing contact angle after 20 min from sample drying. This time was chosen because it corresponds to the transferring time of samples into the humidity chamber (see next section) and the beginning of an experiment. Inside the humidity chamber, samples are no longer exposed to air but to nitrogen plus the adjusted humidity.

**AFM.** The experimental setup has been described in detail before.<sup>7,8</sup> Briefly, our system consists of a commercial AFM with an additional *z* piezoactuator with a high driving frequency, a data-processing and acquisition system, as well as special AFM cantilevers (cantilevers that combine high resonant frequency and low spring constant). Additional modifications were necessary to perform experiments under humid conditions. The current setup contains three additional components: (1) a homemade Teflon humidity chamber, (2) a N<sub>2</sub>/saturated vapor flow ratio controller, and (3) an extended data-processing and fast acquisition system (Figure 2).

To adjust the humidity, a stream of pure nitrogen and a stream of nitrogen saturated with water vapor were mixed, using two mass flow controllers (model GFC, Aalborg). The saturated vapor was obtained by a stream of nitrogen that bubbles through a frit into water. The mixed gas stream was led into the humidity chamber. The humidity was controlled close to the outlet with a sensor (SHT 15, Sensirion, Switzerland). A specially designed humidity chamber with a small volume (approximately 19.7 cm<sup>3</sup>) allows for a fast change in the vapor pressure. Typically, going from low to high humidity and vice versa to dry conditions was

achieved in less than 10 min. The relative humidity is changed, mostly, from 0% up to 90% in steps of 10%.

To reach higher separation rates, we attached an additional *z* piezoactuator (model PL055 PICMA, PI Ceramic, Germany) that is driven by high voltage (up to 80 V) and a high frequency (up to 20 kHz) signal to the AFM. This led us to an extension of the accessible separation rates by up to 4 orders of magnitude (approximately 10<sup>0</sup>–10<sup>7</sup> nm s<sup>−1</sup> in total). Moreover, the actuator provides angstrom resolution and microsecond response, being resistive on water diffusion into the insulation layer under strong humid conditions.

The data-processing and acquisition system is based on a self-written analysis program (LabView 8.5, National Instruments), a data acquisition card (model ATS9462, Alazartech, max. 180 Megasamples per second), a 20 MHz programmable arbitrary waveform generator (model 33220 A, Agilent), and a custom-made high voltage amplifier (built by the electronic workshop of the MPIP, Mainz, Germany).

**Adhesion Force Calculation.** The adhesion force is measured by recording the cantilever deflection during a full approach and retraction cycle (force versus piezo displacement curve); in the following, we call it force curve. The sample is moved up and down by applying a ramp voltage signal to the additional *z* piezoactuator, onto which the sample is mounted. Since the cantilever sensitivity *s* is known, its spring constant *k<sub>c</sub>* multiplied by the cantilever deflection *d* gives the adhesion force, as follows:

$$F_{\text{ad}} = dsk_c \quad (6)$$

While measuring in a force curve cycle, the frequency of full approach and retraction cycle,  $\nu$ , and vertical range of the piezo, *z* (a distance from the noncontact part of force curve to a contact with the sample), are known as well. The separation rate is  $2\nu z$ .

In dynamic force spectroscopy the adhesion force is extracted from force curves and its arithmetic average is plotted as a function of a loading rate  $r_F$ :

$$r_F = 2\nu zk_c \quad (7)$$

To improve the statistics of the measurements and quantify the fluctuation of force curves (pull-off detections), we recorded 20–200 individual force curves for every loading rate. Moreover, the loading rate was varied in a random order to avoid systematic errors in the data associated with SAM deformation and tip wear. A self-written analysis program was used to arithmetically average adhesion force for a proper value of the loading rate. The symmetry of adhesion force distribution was carefully checked and analyzed. Typically, 2500–3000 force curves were used to plot an adhesion histogram.

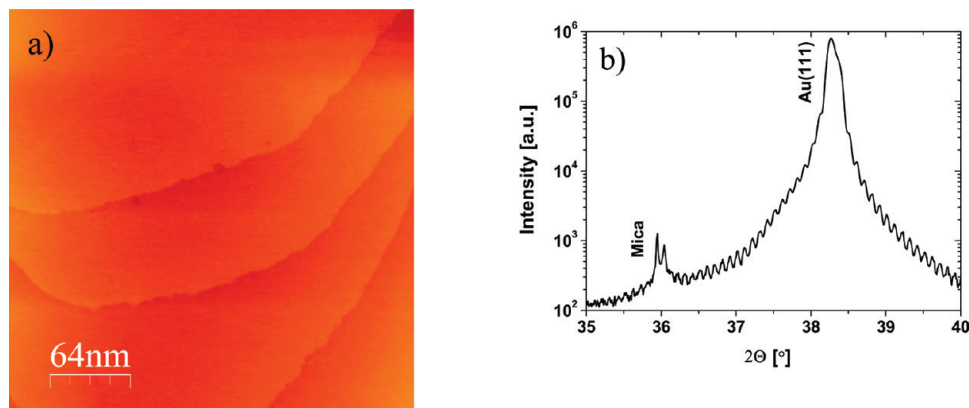
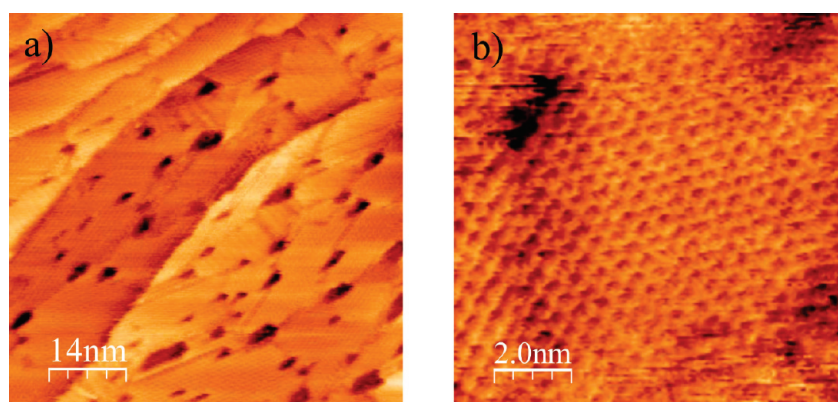
**AFM Cantilevers.** To take full advantage of our modified AFM setup, we had to make a proper choice of AFM cantilevers. First, in order to ensure that the cantilever can follow the high frequency  $\nu$  of ramping the sample up and down, the cantilever resonance frequency has to be significantly larger than  $\nu$  to avoid piezo–cantilever resonance. We found that practically the best choice is to use cantilevers that have roughly 1 order of magnitude higher resonance frequency than  $\nu$ . Second, the cantilever spring constant should be as low as possible to provide high sensitivity for adhesion force measurements. For this reason, we have chosen two types of silicon nitride cantilevers with integrated tips (Table 1).

For cantilever spring constant calibration, we used the thermal noise method that is based on thermal fluctuation of a cantilever.<sup>25</sup> The measurement uncertainty of this method is 10–20%. Preceding each measurement, the cantilevers were cleaned in a plasma cleaner for 25 s (Ar plasma, PDC-001, Harrick Scientific



**Table 1. Mechanical Properties of Used Cantilevers with Tips**

type	description	nominal tip radius [nm]	length [ $\mu\text{m}$ ]	width [ $\mu\text{m}$ ]	thickness [ $\mu\text{m}$ ]	nominal spring constant [ $\text{N m}^{-1}$ ]	nominal resonance frequency [kHz]
1	MLCT-F Veeco Instruments Inc., USA	20	80	14 (width of one leg of triangular cantilever)	0.6	0.50	120
2	OMCL-RC800PSA Olympus, Japan	20	100	40 (rectangular cantilever)	0.8	0.73	71

**Figure 3.** (a) STM height image and (b) XRD of Au(111) on mica. The z-scale in the STM image is 2 nm.**Figure 4.** STM height images of (a) SAM of nonanethiol where the contours of Au(111) terraces are visible and (b)  $(\sqrt{3} \times \sqrt{3})\text{R}30^\circ$  lattice structure of SAM of undecanethiol. The z-scale is encoded from bright to dark and equal to 0.6 nm.

Corporation). Uncoated AFM tips were imaged by a low-voltage scanning electron microscope (SEM, LEO 1530 Gemini, Carl Zeiss NTS, Oberkochen, Germany). From several SEM images, the tip radii were obtained by fitting the circle that coincides with the tip profile (using ImageJ 1.37a software). The measurement uncertainty has been estimated to be 10–20%.

## Results and Discussion

**Characterization of SAMs.** STM images of Au(111) surfaces showed atomically flat terraces with sizes usually exceeding 200 nm in width (Figure 3a). The high Au(111) crystallinity was confirmed by XRD measurements that exhibit a pronounced Au(111) peak (Figure 3b).

$\text{CH}_3$ -terminated SAMs on Au(111) surfaces are well-known to be stable when  $n \geq 7$ . They remain uncontaminated for a long time and could be imaged by STM under ambient conditions. Figure 4a presents a constant current height image of a nonanethiol SAM on Au(111). Five terraces separated by steps of 0.24 nm are visible. Groups of three domains are rotated by around  $120^\circ$  with respect to each other.<sup>16</sup> Randomly distributed depressions (black or darker holes in Figure 4a) with a maximum

average diameter of about 10 nm occur in  $\text{CH}_3$ -terminated SAMs. Their number per unit area and their diameter depend on the self-assembly incubation time, self-assembly incubation temperature, number of  $\text{CH}_2$  groups, and solution concentration. This effect was explained as a corrosion process or reconstruction of the Au(111) surface during adsorption of the thiols.<sup>26,27</sup> The depressions are not deprived of thiol molecules. The molecule position, however, is just lowered by at least one monatomic gold step. Therefore, the depressions are uniform and flat (ordered regions inside the depressions). The maximum depth of depressions according to Figure 4a was measured to be 0.5 nm that corresponds to double Au planes in the (111) direction ( $2 \times 0.24$  nm). The average roughness  $R_a$  measured on  $80 \times 80$  nm<sup>2</sup> terraces was 0.06 nm, including depressions. A similar  $R_a$  value and maximum depth of depressions has been found for all  $\text{HS}-(\text{CH}_2)_n\text{CH}_3$  SAMs for  $n \geq 7$ . For SAMs with  $n \leq 6$ , we could

(26) Schonenberger, C.; Sondaghuehorst, J. A. M.; Jorritsma, J.; Fokkink, L. G. J. *Langmuir* **1994**, *10*, 611–614.

(27) McDermott, C. A.; McDermott, M. T.; Green, J. B.; Porter, M. D. *J. Phys. Chem.* **1995**, *99*, 13257–13267.

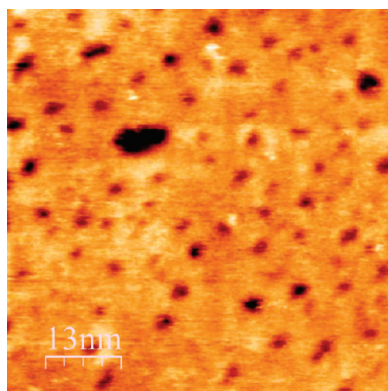


**Figure 5.** STM height images of SAM of mercaptoundecanol. The z-scale is encoded from bright to dark and equal to 1 nm.

not verify the  $(\sqrt{3} \times \sqrt{3})R30^\circ$  hexagonal structure. The depressions were visible. This means that the layer is formed, but its two-dimensional crystallinity is poor.

With the STM, we observed a hexagonal lattice with an intermolecular spacing of 0.5 nm on an undecanethiol SAM on Au(111) (Figure 4b). This is consistent with the  $(\sqrt{3} \times \sqrt{3})R30^\circ$  structure. It corresponds to an area per molecule of 0.216 nm<sup>2</sup>. The  $(\sqrt{3} \times \sqrt{3})R30^\circ$  structure dominates all our prepared CH<sub>3</sub>-terminated SAMs ( $n \geq 7$ ). STM imaging of samples was repeated after 48 h, and no characteristic changes were observed after this time.

As reported by other groups,<sup>17,18,28</sup> the OH-terminated SAMs could only be imaged by using the STM either in electrolytes or in an ultrahigh vacuum. In air, we could not achieve atomic resolution (Figure 5). The characteristic depressions, however, were observed on the scanned surfaces. The number of depressions per unit area was indistinguishable to the ones observed for CH<sub>3</sub>-terminated SAMs.

Liu et al.<sup>17</sup> recently showed that SAMs of mercaptohexanol undergo a transformation to a condensed and stable structure, identified as  $c(3 \times 2\sqrt{3})$  (which describes equivalent to a  $c(4 \times 2)$  superlattice with respect to the  $(\sqrt{3} \times \sqrt{3})R30^\circ$  hexagonal structure). The corresponding lattice constants were shown to be 0.87 and 1.01 nm (corresponding to 3 and  $2\sqrt{3}$  times the intermolecular spacing of the Au(111)) where one unit cell contains four molecules. This results in an area per molecule of 0.217 nm<sup>2</sup>. This is almost identical to the area per molecule for the  $(\sqrt{3} \times \sqrt{3})R30^\circ$  hexagonal structure.

Yang et al.<sup>18</sup> have, however, shown that molecules of SAMs of mercaptoundecanol adopt a  $(\sqrt{3} \times \sqrt{3})R30^\circ$  hexagonal lattice. Based on analogy to CH<sub>3</sub>-terminated SAMs (for  $n \geq 7$ ), we assume that the SAMs of mercaptononanol and mercaptohexadecanol form a  $(\sqrt{3} \times \sqrt{3})R30^\circ$  hexagonal lattice as well.

For CH<sub>3</sub>-terminated SAMs, the advancing contact angle increases with increasing length of alkyl chain, that is, thickness of SAMs (Figure 6). The thickness was calculated theoretically for a close-packed monolayer tilted 30° from the normal.<sup>19</sup> This observation agrees with what has been reported in the literature.<sup>20,29</sup> The effect is explained by the increasing stability and order of the monolayer with the growing film thickness. The same effect of increasing stability and order is responsible for the inverted tendency found for OH-terminated SAMs exceeding a thickness of 1.4 nm ( $n = 9$ ). In this case, the polar OH groups can better interact with water, which results in the decreasing contact angle.

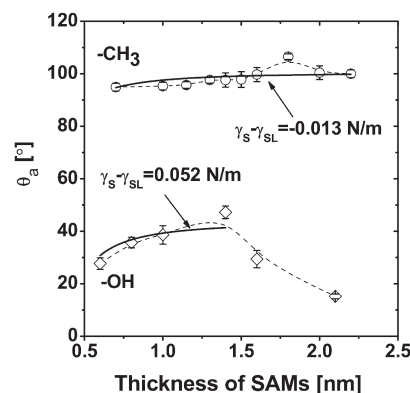


**Figure 6.** Advancing contact angle ( $\theta_a$ ) as function of thickness of SAMs. Error bars indicate the standard deviation of the measurement. The solid lines are the fits with Young's equation including van der Waals interaction between gold and a water drop. The dashed lines are to guide the eye.

However, below a monolayer thickness of 1.4 nm, the tendency is changed. We attribute this to increasing van der Waals interaction between the water and the gold for decreasing monolayer thickness.

To take the influence of the van der Waals forces between water and gold across SAMs into account we added a term in the Young's equation:

$$\gamma_L \cos \theta_a = \gamma_S - \gamma_{SL} + \frac{A_{H(Au/HC/water)}}{12\pi D_0^2} \quad (8)$$

Here,  $\gamma_L$ ,  $\gamma_S$ , and  $\gamma_{SL}$  are the interfacial tensions of water–air ( $\gamma_L = 0.072 \text{ N m}^{-1}$ ), monolayer–air, and water–monolayer, respectively, for an infinitely thick film.  $A_{H(Au/HC/water)}$  is the Hamaker constant for gold/hydrocarbon/water, and  $D_0$  is the thickness of the monolayer. For the Hamaker constant estimation for gold/hydrocarbon/water, we used the combining relation of  $A_{132} = (A_{131}A_{232})^{1/2}$  and  $A_{131} = A_{313}$ . Here, indexes 1, 2, and 3 indicate different media. Since we could not find Hamaker constants of Au/hydrocarbon/Au in the literature, we used Au/ethanol/Au as a rough estimate ( $A_{H(Au/ethanol/Au)} = 40 \text{ zJ}$ ).<sup>30</sup> Hamaker constants of hydrocarbons interacting across water are all close to 4 zJ.<sup>31</sup> We estimated the  $A_{H(Au/HC/water)}$  value to be  $13 \times 10^{-21} \text{ J}$ . The difference,  $\gamma_S - \gamma_{SL}$ , can be calculated by fitting (solid lines in Figure 6) with eq 8. We found that  $\gamma_S - \gamma_{SL} = -0.013 \text{ N m}^{-1}$  and  $\gamma_S - \gamma_{SL} = 0.052 \text{ N m}^{-1}$  for CH<sub>3</sub>- and OH-terminated SAMs, respectively. The values agree with the literature (for liquids of alkyl hydrocarbons and fatty alcohols, respectively).<sup>32</sup> We estimated an error of the fit to be 25–35% including an uncertainty in  $A_{H(Au/HC/water)}$ .

Since in our case the measurements of the dynamic force spectroscopy had to be performed for a few hours, we also checked the stability of the advancing contact angle. We observed that the contact angle within 2 h increases maximum 7° beyond the results shown in Figure 6 for OH-terminated SAMs, while for CH<sub>3</sub>-terminated SAMs the contact angle remains stable.

**Adhesion Force Distributions.** In Figure 7a, the variation of adhesion force is presented as one example of nonanethiol SAMs at different loading rates.  $N = 3000$  force curves were recorded and evaluated. The maximal load was fixed to 30 nN. The interval

(30) Kane, V.; Mulvaney, P. *Langmuir* **1998**, *14*, 3303–3311.

(31) Drummond, C. J.; Georgaklis, G.; Chan, D. Y. C. *Langmuir* **1996**, *12*, 2617–2621.

(32) Israelachvili, J. *Intermolecular and surfaces forces*, 2nd ed.; Academic Press: London, 1992.

(28) Poirier, G. E.; Pylant, E. D.; White, J. M. *J. Chem. Phys.* **1996**, *105*, 2089–2092.

(29) Ederth, T. J. *Phys. Chem. B* **2000**, *104*, 9704–9712.

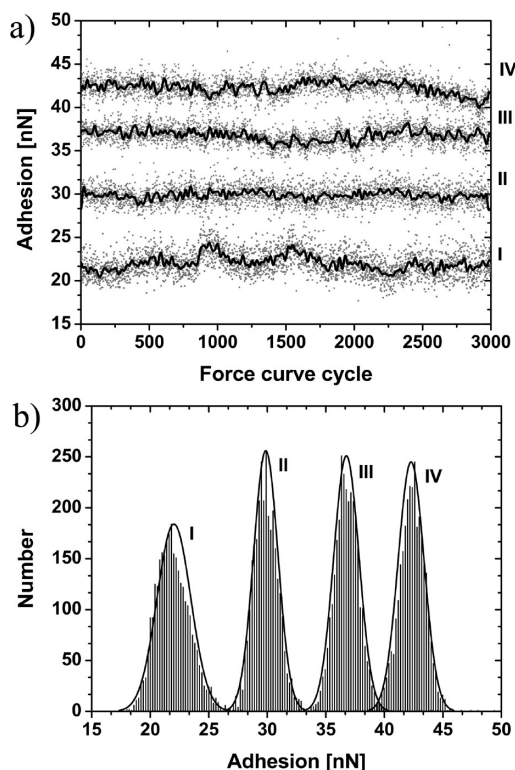


**Figure 7.** (a) Adhesion force (gray dots) measured versus force curve cycle between nonanethiol SAM and  $\text{Si}_3\text{N}_4$  tip. Solid curves were obtained by a five-point FFT smoothing of the original curves. The four traces were recorded at different loading rates: (I)  $9.7 \times 10^3 \text{ nN s}^{-1}$ , (II)  $287 \times 10^3 \text{ nN s}^{-1}$ , (III)  $923 \times 10^3 \text{ nN s}^{-1}$ , and (IV)  $2600 \times 10^3 \text{ nN s}^{-1}$ . The mean value of adhesion including standard deviation of the mean: (I)  $22.0 \pm 1.4 \text{ nN}$ , (II)  $29.9 \pm 1.0 \text{ nN}$ , (III)  $36.8 \pm 1.1 \text{ nN}$ , and (IV)  $42.3 \pm 1.1 \text{ nN}$ . (b) Typical force curves. Gauss curves were fitted to the experimental results. Panels (a) and (b) refer to the same experiment. The relative humidity is 10%.

time (time between each force curve cycle) was 100 ms. Adhesion forces did not systematically change with time. Farshchi-Tabrizi et al.<sup>33</sup> have analyzed the source of variations in adhesion force experiments. Two kinds of variations can be distinguished: a random fluctuation from one force curve to the other (“random noise”) and variations on a slower time scale of  $\sim 10 \text{ s}$  which are visible after smoothing of the data (solid curves).

The corresponding histograms of the adhesion forces revealed symmetrical distributions (Figure 7b). In some cases, small deviations were observed for small loading rates (see histogram I). Since the adhesion force distributions are essentially symmetric, there was no need to differentiate between average adhesion force (numeric mean of all values) and the most probable force (peak position of the distribution), and the average value was used in all calculations.

No strong influence of load on adhesion on monolayers was found (not shown). We could only observe a minor increase of adhesion versus load for thin and intermediate monolayers (for  $\text{CH}_3$ -terminated SAMs,  $n \leq 8$ ; for OH-terminated SAMs,  $n \leq 9$ ) when the applied load exceeded approximately 160 nN within the range of 5–300 nN and 5–600 nN for  $\text{CH}_3$ - and OH-terminated SAMs, respectively (the upper load range was limited by the voltage applied to the additional piezoactuator, and it was

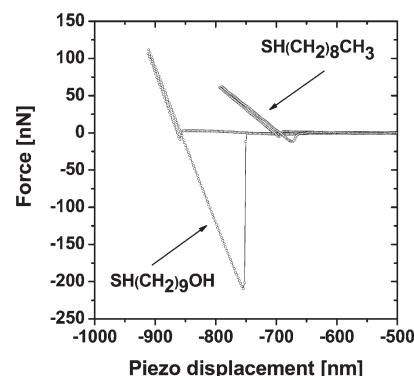


**Figure 8.** Force curves taken on SAMs of nonanethiol (cantilever type 2) and mercaptononanol (cantilever type 1) at a loading rate of  $r_F \approx 10^4 \text{ nN s}^{-1}$  and relative humidity of 40%.

different in the cases of  $\text{CH}_3$ - and OH-terminated SAMs due to significant differences in value of adhesion).

In Figure 8, single force curves for nonanethiol and mercaptononanol are presented. In all experiments, the applied load was kept constant and never exceeded 140 and 150 nN for  $\text{CH}_3$ -terminated SAMs and OH-terminated SAMs, respectively. These forces did not lead to molecular packing changes in the monolayers, since so-called “pop-in” phenomena was not observed.<sup>15,21</sup>

#### Dynamic Force Spectroscopy of $\text{CH}_3$ -Terminated SAMs.

For  $\text{CH}_3$ -terminated SAMs, adhesion increased monotonically with increasing loading rate in the range from 10 to  $10^7 \text{ nN s}^{-1}$ . Results of five typical experiments are shown in Figure 9. When the number of  $\text{CH}_2$  groups is changed ( $n = 6$ –15), the thickness of the monolayer varies from 1.0 to 2.0 nm.<sup>19</sup> The chain length had no significant influence on the adhesion force (for  $n \geq 8$ ). This agrees with results of Subramanian and Sampath.<sup>22</sup> For low loading rates, the observed adhesion forces were  $(12 \pm 4) \text{ nN}$ . The error refers to the variation from one experiment to the next. Normalizing by the radius of curvature leads to an adhesion force of  $(0.4 \pm 0.1) \text{ N m}^{-1}$ .

For hexanethiol SAMs ( $n = 6$ ), higher adhesion was observed. We attribute this high adhesion to the lower degree of stability in the short-chain alkanethiol under the pressure exerted by the tip and the resulting energy dissipation. The van der Waals attraction between these shorter alkyl chains is too weak to stabilize the two-dimensional crystalline structure under the applied load.

Two regimes can be identified in the adhesion versus loading rate curves. First, the adhesion increases weakly with the logarithm of loading rate. This weak increase dominates up to  $\sim 10^4 \text{ nN s}^{-1}$ . Then after a transition regime from  $\sim 10^4$  to  $\sim 10^5 \text{ nN s}^{-1}$ , the adhesion increases steeply, starting from the loading rate of about  $10^5 \text{ nN s}^{-1}$ . We take this as an indication that the separation of the surface is governed by two different processes.

Adhesion forces measured at 10% relative humidity were fitted with the Bell–Evans model. An example is shown in Figure 10a. At such low humidity, capillary forces were minimized.<sup>23</sup> The fitting was carried out for the two regimes separately. We omitted the transition points between the regimes and some points for very high loading rate that do not follow the tendency. The resulting fit parameters are listed in Table 2. Fitting with more than two regimes did not improve the fit accuracy. The linear increase of adhesion force with the logarithm of the loading rate indicates that the Bell–Evans model, developed for a single bond, can be also applied for multibond adhesion. This means that multibond adhesion can be summarized into one effective bond adhesion (one tip–sample interaction potential), where bonds within a nanocontact are not considered individually.

(33) Farshchi-Tabrizi, M.; Kappl, M.; Cheng, Y. J.; Gutmann, J.; Butt, H. J. *Langmuir* **2006**, *22*, 2171–2184.



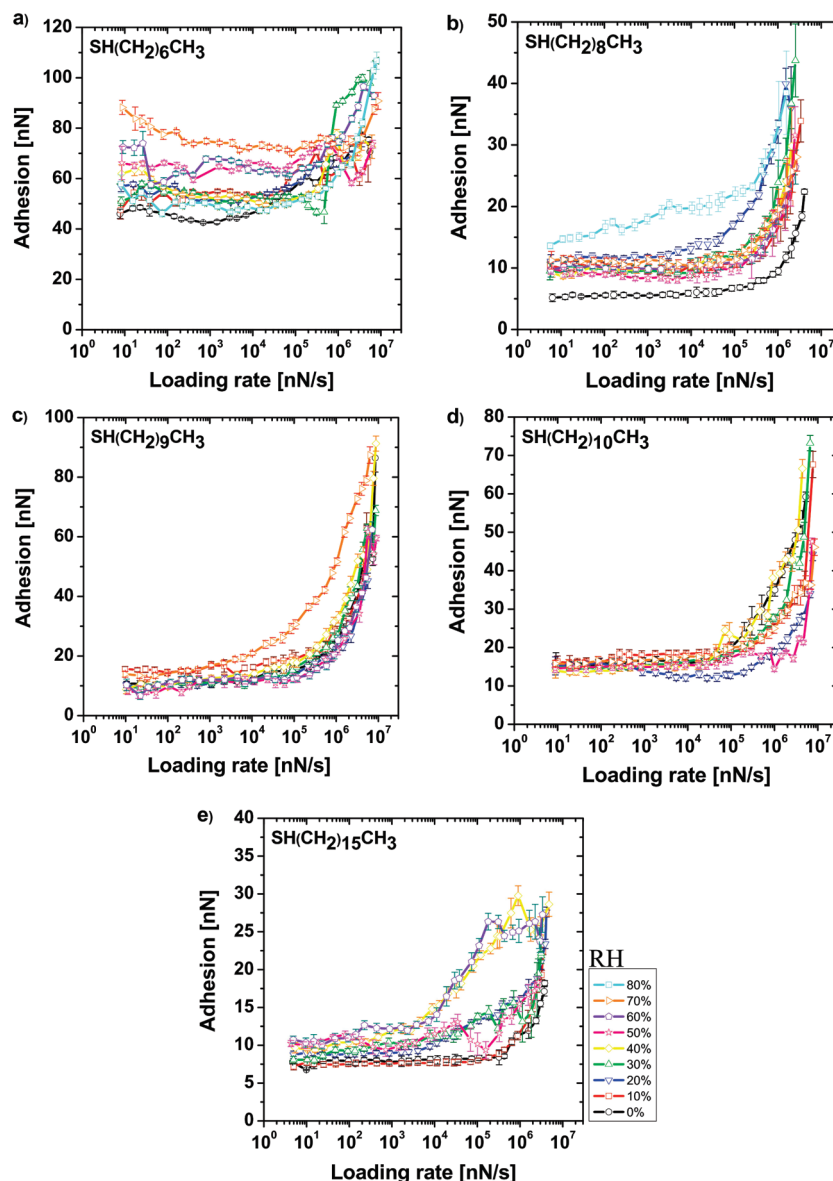


**Figure 9.** Representative adhesion versus loading rate curves between CH<sub>3</sub>-terminated SAMs and a Si<sub>3</sub>N<sub>4</sub> AFM tip at different humidity. The error bars indicate the standard deviation of the mean. The five experiments were carried out with tips having radii of 23–41 nm.

The two regimes in the  $F_{\text{ad}}$  versus  $\ln r_F$  correspond to two energy barriers that hinder separation. Each of the barriers should reflect a different type of adhesive interaction that contributes to the effective bond. We calculated kinetics and barrier parameters for both contributions (Table 2). The distance between the bound state and the transition state (see Figure 1),  $x_\beta$ , was calculated from the slope ( $F_\beta = k_B T/x_\beta$ ) of the dependence,  $F_{\text{ad}} = F_\beta \ln r_F - b$ , and the dissociation constant,  $k_{\text{off}}^0$ , from the intercept ( $b = F_\beta \ln(F_\beta k_{\text{off}}^0)$ ).

The activation length for the first regime,  $x_\beta^{(1)}$ , ranges between 11 and 100 pm (Table 2). This is of the same order as typical interatomic distances. Lifetimes of the undisturbed bond range between  $8 \times 10^{21}$  and  $8 \times 10^{103}$  s. This implies that the bond related to the first regime is thermally stable. Practically, a spontaneous breakage will not happen. We did not notice systematic variations with the chain length as long as  $n \geq 8$ . We attribute the first process to attractive van der Waals forces, since these are expected to give the dominant contribution to static adhesion in this system.

The second type of interaction is thermally much less stable and becomes limiting only at high loading rates. Activation lengths for

the second regime,  $x_\beta^{(2)}$ , are in the range of 0.26–1.0 pm. Bond lifetimes are in the order of few 10  $\mu$ s to few 10 s. From control experiments on the bare gold substrate and from comparison with the experiments on OH-terminated thiols, it is clear that this second regime occurs only in the presence of the thiol monolayer and that it depends on the molecular end group of the surface. However, we cannot deduce a more detailed molecular picture of the origin of this second regime from our measurements.

The results for the heptanethiol SAM varied significantly from experiment to experiment. For this reason, we did not further analyze them.

Spontaneous breakage of effective bonds mediated by the second type of interaction can happen within less than 1 ms just by thermal fluctuation of the system. This interaction is therefore not stable enough to play a role for static situations. It would, for example, be irrelevant for the adhesion force in a powder sample. If, however, we are considering processes occurring on such short time scales such as rapid flow of powders or a particle impacting another particle, interaction forces should be dominated by this second type of interaction.



**Table 2.** Kinetic and Interaction Potential Parameters Including Thermal Fluctuation Force  $F_\beta$  and Intercept  $b$  for CH<sub>3</sub>-Terminated SAM Samples at 10% Relative Humidity As Obtained from Fit of the Experimental Data Using the Bell–Evans Model (See eq 4)<sup>a</sup>

sample	regime	$F_\beta$ [nN]	$b$ [nN]	$x_\beta$ [pm]	$r_F^0$ [nN s <sup>-1</sup> ]	$k_{\text{off}}^0$ [s <sup>-1</sup> ]	$t_{\text{off}}^0$ [s]	$\Delta E_0$ [J]
HS(CH <sub>2</sub> ) <sub>6</sub> CH <sub>3</sub>	1	0.37	-50.6	11	$4 \times 10^{-60}$	$1 \times 10^{-59}$	$9 \times 10^{58}$	$5.3 \times 10^{-19}$
	2	3.9	-9	1.0	$1 \times 10^{-1}$	$3 \times 10^{-2}$	$4 \times 10^1$	
HS(CH <sub>2</sub> ) <sub>8</sub> CH <sub>3</sub>	1	0.04	-9.7	100	$5 \times 10^{-106}$	$1 \times 10^{-104}$	$8 \times 10^{103}$	$10 \times 10^{-19}$
	2	15.3	199	0.26	$5 \times 10^5$	$3 \times 10^4$	$3 \times 10^{-5}$	
HS(CH <sub>2</sub> ) <sub>9</sub> CH <sub>3</sub>	1	0.1	-14.8	41	$5 \times 10^{-65}$	$5 \times 10^{-64}$	$2 \times 10^{63}$	$6.2 \times 10^{-19}$
	2	9.2	100	0.44	$5 \times 10^4$	$5 \times 10^3$	$2 \times 10^{-4}$	
HS(CH <sub>2</sub> ) <sub>10</sub> CH <sub>3</sub>	1	0.30	-15.5	13	$4 \times 10^{-23}$	$1 \times 10^{-22}$	$8 \times 10^{21}$	$2.3 \times 10^{-19}$
	2	6.18	59.3	0.65	$2 \times 10^4$	$2 \times 10^3$	$4 \times 10^{-4}$	
HS(CH <sub>2</sub> ) <sub>15</sub> CH <sub>3</sub>	1	0.043	-7.33	94	$9 \times 10^{-75}$	$2 \times 10^{-73}$	$5 \times 10^{72}$	$7.2 \times 10^{-19}$
	2	7.6	93	0.53	$2 \times 10^5$	$3 \times 10^4$	$4 \times 10^{-5}$	

<sup>a</sup>  $x_\beta$  = the distance between the bound state and the transition state,  $r_F^0$  = the thermal loading rate,  $k_{\text{off}}^0$  = the thermal dissociation constant, and  $t_{\text{off}}^0$  = the bond lifetime.  $\Delta E_0 = E_0^{(1)} - E_0^{(2)}$ , where  $E_0^{(1)}$  and  $E_0^{(2)}$  represent the energy barriers “1” and “2”, respectively.

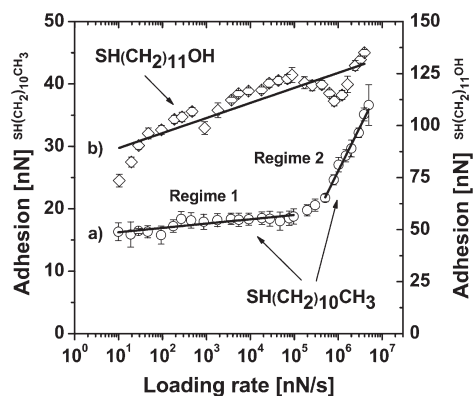


**Figure 10.** Adhesion force versus loading rate curve between (a) SAM of undecanethiol and Si<sub>3</sub>N<sub>4</sub> tip, and (b) SAM of mercaptoundecanol and Si<sub>3</sub>N<sub>4</sub> tip for 10% and 0% relative humidity, respectively. The error bars were calculated as a standard deviation of mean. The lines are the fits with the Bell–Evans model. Two fitting regimes for (a): (1) loading rates from 10 to 10<sup>5</sup> nN s<sup>-1</sup> and (2) loading rates from 5 × 10<sup>5</sup> to 5 × 10<sup>6</sup> nN s<sup>-1</sup>. One fitting regime for (b): loading rates from 10 to 4 × 10<sup>6</sup> nN s<sup>-1</sup>.

To estimate the number of molecules taking part in each tip–sample contact, we used the Johnson–Kendall–Roberts<sup>34</sup> (JKR) model. In the JKR model, the adhesive interaction between a sphere and a homogeneous elastic half space with a planar surface is considered. The contact area is calculated from the elastic deformation of the contact due to the externally force and the adhesion force. The work of adhesion,  $W$ , can be calculated from the adhesion force, if the tip radius,  $R$ , is known:

$$W = \frac{2F_{\text{ad}}}{3\pi R} \quad (9)$$

The radius of the contact area at separation (separation contact radius),  $a$ , in the JKR theory is given as

$$a = \left( \frac{3\pi R^2 W}{2E} \right)^{1/3} \quad (10)$$

Here,  $E$  is the elastic modulus of the alkanethiol monolayer coated gold. Different values of the elastic modulus can be found in the

literature depending on simulations<sup>35</sup> or measurements.<sup>36,37</sup> A value of  $E = 20 \pm 10$  GPa was found by Leng and Jiang<sup>35</sup> for CH<sub>3</sub>-terminated SAMs in molecular dynamics simulations. We assume the same value for OH-terminated SAMs as well. This value of the elastic modulus did not depend on the chain length of the molecules.

Equation 10 is valid for the force exerted by a tip at negative load (jump-off contact). During unloading, a neck that links the tip and sample is abruptly released. The separation occurs when the radius of the contact area has fallen to be smaller of a factor 0.25<sup>1/3</sup> in relation to the radius of the contact area at zero force.<sup>38</sup> When the force exerted by a tip is positive, the contact radius,  $a$ , and indentation,  $\delta$ , reach the maximum at applied force,<sup>34</sup>  $F_{\text{max}}$ :

$$a = \sqrt[3]{\frac{R}{E} \left( F_{\text{max}} + 3\pi R W + \sqrt{6\pi R W F_{\text{max}} + (3\pi R W)^2} \right)} \quad (11)$$

$$\delta = \frac{a^2}{R} - \frac{2}{3} \sqrt{\frac{6\pi W a}{E}} \quad (12)$$

The radii of the AFM tips were calculated from SEM images which were taken after the adhesion experiments. We have not observed any difference using tip type 1 and 2 while performing dynamic force spectroscopy measurements.

Tip radii for the four typical experiments as well as calculations using the JKR model are listed in Table 3. For a hexagonal structure with a lattice constant of 0.5 nm, the area per molecule is 0.22 nm<sup>2</sup>. For the four chosen examples, the work of adhesion varied between 0.045 and 0.113 N m<sup>-1</sup>. The separation contact radii from 2.3 to 3.2 nm and the number of molecules in the contact area ranged from 75 to 148.

Humidity only has little influence on the adhesion, in particular not for loading rates up to 10<sup>4</sup> nN s<sup>-1</sup>. This is not surprising, since meniscus formation is not expected for this type of surface because the contact angle of water on the alkyl thiols is greater than 90°. As a result, capillary forces should be negligible.<sup>23</sup> At high loading rates, there are, however, some systematic humidity effects. First, at a relative humidity above 70–80%, adhesion increases (e.g., Figure 9b and c). Second, the slope of the  $F_{\text{ad}}$  versus  $\ln r_F$  curve in the first regime tended to increase with increasing loading rate. We attribute these effects to an increased amount of water adsorbed to the tip surface. At high humidity, a tip with an adsorbed layer of water interacts with the SAMs, while at low humidity the silicon nitride surface interacts directly.

(34) Johnson, K. L.; Kendall, K.; Roberts, A. D. *Proc. R. Soc. London, Ser. A* **1971**, 324, 301–313.

(35) Leng, Y. S.; Jiang, S. Y. *J. Chem. Phys.* **2000**, 113, 8800–8806.

(36) Burns, A. R.; Houston, J. E.; Carpick, R. W.; Michalske, T. A. *Phys. Rev. Lett.* **1999**, 82, 1181–1184.

(37) Kiriden, W.; Jain, V.; Kuo, P. K.; Liu, G. Y. *Surf. Interface Anal.* **1997**, 25, 383–389.

(38) Butt, H. J.; Cappella, B.; Kappl, M. *Surf. Sci. Rep.* **2005**, 59, 1–152.

**Table 3. Radius of Four AFM Tips Used in Four Typical Experiments on CH<sub>3</sub>-Terminated SAMs and Calculations Using the JKR Model**

sample	used tip	tip radius [nm]	applied force [nN] <sup>a</sup>	work of adhesion [mN m <sup>-1</sup> ] <sup>b</sup>	separation contact radius [nm]	indentation [nm]	no. of molecules in contact area
HS(CH <sub>2</sub> ) <sub>8</sub> CH <sub>3</sub>	type 2	23	55	96	2.3	0.8	75
HS(CH <sub>2</sub> ) <sub>9</sub> CH <sub>3</sub>	type 1	29	139	113	2.8	1.2	113
HS(CH <sub>2</sub> ) <sub>10</sub> CH <sub>3</sub>	type 1	41	130	84	3.2	1.1	148
HS(CH <sub>2</sub> ) <sub>15</sub> CH <sub>3</sub>	type 2	34	67	45	2.3	0.7	76

<sup>a</sup> The applied load was averaged for the whole range of loading rate. The relative humidity is 10%. <sup>b</sup> The adhesion values at the lowest loading rate only were taken for the calculation.

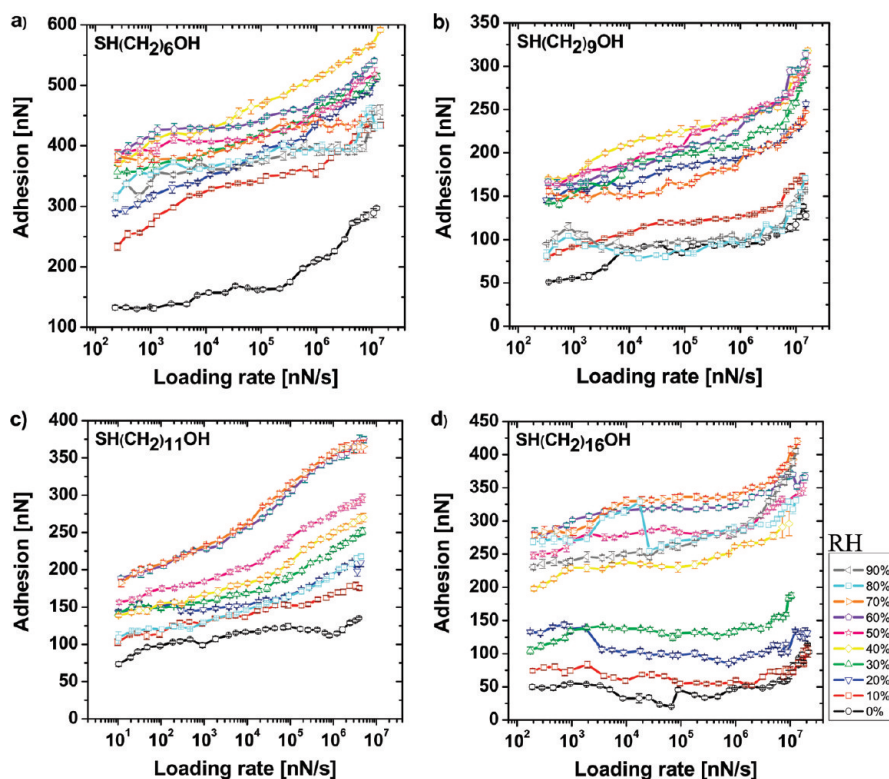


**Figure 11.** Representative adhesion versus loading rate curves between OH-terminated SAMs and a Si<sub>3</sub>N<sub>4</sub> AFM tip at different humidity. The error bars indicate the standard deviation of the mean. The four experiments were carried out with tips having radii of 20–43 nm.

### Dynamic Force Spectroscopy of OH-Terminated SAMs.

The hydroxyl end group of thiol molecules changes the surface to be hydrophilic ( $\theta_a < 90^\circ$ ). We again show results of four typical experiments in Figure 11. Even at zero humidity and slow loading rates, the mean adhesion is roughly 6 times higher on the OH-terminated SAMs than on the CH<sub>3</sub>-terminated ones. In addition, adhesion forces on OH-terminated SAMs depended more sensitively on the loading rate than adhesion forces on CH<sub>3</sub>-terminated SAMs in the first regime. As a first approximation, the adhesion force increased linearly with the logarithm of the loading rate. The slope of this increase changed with the humidity. The slope increased at low humidity, was maximal in the intermediate regime, and decreased again at high humidity.

For loading rates at or above  $10^7$  nN s<sup>-1</sup>, we sometimes observed a steeper increase of the adhesion versus the loading rate (e.g., Figure 11b and d). It was not systematically correlated to the humidity.

In earlier experiments between two silicon oxide or silicon nitride surfaces, significant wear of the tip was observed, in particular after experiments at high humidity.<sup>33</sup> We inspected all tips by SEM after the experiment. No changes in the shape or tip radius were detected when comparing to the tip before the experiment. Thus, wear is negligible on thiol monolayers. We speculate that one reason for the negligible wear is the high elastic

**Table 4. Kinetic and Interaction Potential Parameters Including Thermal Fluctuation Force  $F_\beta$  and Intercept  $b$  for OH-Terminated SAM Samples at 0% Relative Humidity As Obtained from Fit of the Experimental Data Using the Bell-Evans Model (See eq 4)<sup>a</sup>**

sample	$F_\beta$ [nN]	$b$ [nN]	$x_\beta$ [pm]	$r_F^0$ [nN s <sup>-1</sup> ]	$k_{\text{off}}^0$ [s <sup>-1</sup> ]	$t_{\text{off}}^0$ [s]
HS(CH <sub>2</sub> ) <sub>6</sub> -OH	12.5	-41.3	0.33	$4 \times 10^{-2}$	$3 \times 10^{-3}$	$3 \times 10^2$
HS(CH <sub>2</sub> ) <sub>9</sub> -OH	5.3	-25.7	0.77	$8 \times 10^{-3}$	$1 \times 10^{-3}$	$7 \times 10^2$
HS(CH <sub>2</sub> ) <sub>11</sub> -OH	3.1	-81.9	1.3	$8 \times 10^{-12}$	$2 \times 10^{-12}$	$4 \times 10^{11}$
HS(CH <sub>2</sub> ) <sub>16</sub> -OH	0.25	-42.2	16	$5 \times 10^{-74}$	$2 \times 10^{-73}$	$5 \times 10^{72}$

<sup>a</sup>  $x_\beta$  = the distance between the bound state and the transition state,  $r_F^0$  = the thermal loading rate,  $k_{\text{off}}^0$  = the thermal dissociation constant, and  $t_{\text{off}}^0$  = the bond lifetime.

deformability of the thiol layer as compared to silicon oxide or nitride. As a result, the maximal stress occurring in the contact area is reduced and stress peaks are smeared out. That the stress is reduced is obvious from eq 11. For a lower elastic modulus, the contact area increases and thus the load is distributed over a larger area. This leads to lower maximal pressure and to lower pressure gradients in the contact area. In addition, on the nanoscale, the surface of the tip is not a perfect, continuous spherical object. It

**Table 5. Radius of Four AFM Tips Used in Four Typical Experiments on OH-Terminated SAMs and Calculations Using the JKR Model<sup>a</sup>**

sample	tip radius [nm]	applied force [nN] <sup>b</sup>	work of adhesion [mN m <sup>-1</sup> ] <sup>c</sup>	separation contact radius [nm]	indentation [nm]	no. of molecules in contact area
HS(CH <sub>2</sub> ) <sub>6</sub> OH	43	72	653	6.6	1.2	618
HS(CH <sub>2</sub> ) <sub>9</sub> OH	26	115	420	4.1	1.3	235
HS(CH <sub>2</sub> ) <sub>11</sub> OH	25	31	625	4.5	0.9	291
HS(CH <sub>2</sub> ) <sub>16</sub> OH	20	95	529	3.7	1.3	193

<sup>a</sup> Used tip: type 1. <sup>b</sup> The applied load was averaged for the whole range of loading rate. The relative humidity is 10%. <sup>c</sup> The adhesion values at the lowest loading rate only were taken for the calculation.

will be rough and not homogeneous. As a result, the stress around asperities might be significantly higher than one would estimate with continuum theory. The soft thiol monolayer would avoid such stress peaks.

Adhesion forces measured at completely dry conditions (relative humidity = 0%) are fitted with the Bell–Evans model (see example in Figure 10b). We have omitted data points beyond loading rates of  $5 \times 10^6$  nN s<sup>-1</sup>. Fitting was carried out assuming only one regime, since there is no strong evidence for the existence of two or more regimes. The resulting fit and kinetic parameters are listed in Table 4. The activation length ranges between 0.33 and 16 pm. Lifetimes of the bond range between  $3 \times 10^2$  and  $5 \times 10^{72}$  s. We observed systematic variations with the chain length in this case. It can be seen that the activation length and durability of the effective bond are increasing with monolayer thickness. The logarithm of the bond lifetime scales almost linearly with the monolayer thickness. There is no such linear scaling between the logarithm of the activation length and the monolayer thickness. For the chain length  $n \geq 11$ , bond lifetimes are too high to observe spontaneous breakage by thermal activation in practice.

Calculation using the JKR model as well as tip radii for the four typical experiments are listed in Table 5. The work of adhesion varied between 0.420 and 0.653 N m<sup>-1</sup>. The separation contact radii ranged from 3.7 to 6.6 nm, and the number of molecules in the contact area ranged from 193 to 618. The large values of contact radii and number of molecules in the adhesive contact compared to CH<sub>3</sub>-terminated SAMs (Table 3) explain, partially, the big value of adhesion force (Figure 11). This can be best seen for mercaptohexanol (Figure 11a and Table 5).

We have yet no good explanation for the 6 times stronger adhesion observed on OH-terminated thiols as compared to CH<sub>3</sub>-terminated thiols. Continuum van der Waals forces should not be so much different because they are longer ranged and do not so much depend on one atomic layer. Hydrogen bridges between silanol groups on the tip and hydroxyl groups on the monolayer most likely contribute significantly. This interpretation agrees also with the strong dependence on the loading rate. Hydrogen bridges are expected to depend more sensitively on separation than van der Waals forces, which would explain the shorter activation lengths. A simple estimation, however, shows that hydrogen bonds are most likely not sufficient to explain the strong adhesion. By subtracting the mean adhesion force measured on CH<sub>3</sub>-terminated thiols from the mean adhesion force measured on OH-terminated thiols, we estimate the hypothetical contribution of hydrogen bonds to be 45 nN. An upper limit of the number of contributing hydrogen bonds would be in the order of 600 (see Table 5), which is probably a strong overestimate. This would correspond to an adhesion force of at least 75 pN per

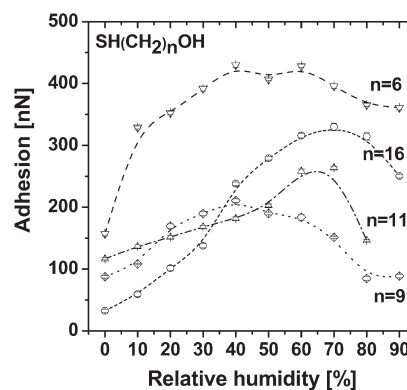


**Figure 12.** Adhesion force versus relative humidity for OH-terminated SAMs. The same four examples were chosen as in Figure 11. The adhesion values for a loading rate of about  $10^4$  nN s<sup>-1</sup> are plotted. The dashed and dotted curves are guides to the eye.

hydrogen bond. While in some publications rupture forces of more than 100 pN have been reported,<sup>39–41</sup> recent estimates give values of only a few pN per hydrogen bond.<sup>42,43</sup> Therefore, we conclude that the strong adhesion between the OH groups of the SAM and the silicon nitride tips cannot be explained by hydrogen bonding and is thus not fully understood.

Adhesion forces on OH-terminated SAMs depended sensitively on humidity (Figure 12). At low humidity, the adhesion force increased, reached a maximum at an intermediate humidity, and decreased again at very high humidity. The humidity at the maximum varied from experiment to experiment. This effect was shown already in many papers, describing the adhesion–humidity relation for AFM tip–hydrophilic samples.<sup>6,33,44–46</sup> Such a dependence can be explained by capillary forces, that increase at low humidity due to surface roughness<sup>47</sup> (tip surface roughness in our case) and decrease at very high humidity due to the small size of the AFM tip; a decrease of the capillary force at high humidity is expected for nanosized spheres.<sup>33,48</sup>

One possible reason for the rate dependence of adhesion forces on OH-terminated thiols could be the condensation and evaporation time of the water meniscus. Based on a calculation of Kohonen et al.,<sup>49</sup> one can derive a characteristic condensation/evaporation

(39) Williams, J. M.; Han, T. J.; Beebe, T. P. *Langmuir* **1996**, *12*, 1291–1295.

(40) Wenzler, L. A.; Moyes, G. L.; Raikar, G. N.; Hansen, R. L.; Harris, J. M.; Beebe, T. P.; Wood, L. L.; Saavedra, S. S. *Langmuir* **1997**, *13*, 3761–3768.

(41) Grubmüller, H.; Heymann, B.; Tavan, P. *Science* **1996**, *271*, 997–999.

(42) Janke, M.; Rudzevich, Y.; Molokanova, O.; Metzroth, T.; Mey, I.; Diezemann, G.; Marszałek, P. E.; Gauss, J.; Bohmer, V.; Janshoff, A. *Nat. Nanotechnol.* **2009**, *4*, 225–229.

(43) Onoa, B.; Dumont, S.; Liphardt, J.; Smith, S. B.; Tinoco, I.; Bustamante, C. *Science* **2003**, *299*, 1892–1895.

(44) Wei, Z.; Zhao, Y. P. *J. Phys. D: Appl. Phys.* **2007**, *40*, 4368–4375.

(45) Asay, D. B.; Kim, S. H. *J. Chem. Phys.* **2006**, *124*, 174712.

(46) Jang, J.; Yang, M.; Schatz, G. J. *J. Chem. Phys.* **2007**, *126*, 174705.

(47) Butt, H. J. *Langmuir* **2008**, *24*, 4715–4721.

(48) Pakarinen, O. H.; Foster, A. S.; Paajanen, M.; Kalinainen, T.; Katainen, J.; Makkonen, I.; Lahtinen, J.; Nieminen, R. M. *Modell. Simul. Mater. Sci. Eng.* **2005**, *13*, 1175–1186.

(49) Kohonen, M. M.; Maeda, N.; Christenson, H. K. *Phys. Rev. Lett.* **1999**, *82*, 4667–4670.



time of the liquid meniscus between a sphere of radius  $R$  and a planar surface.<sup>23</sup>

$$\tau = -\frac{\rho R_g T R \lambda_K}{D M_w P \ln(P/P_0)} \quad (13)$$

Here,  $\rho$  is the density of the liquid,  $R_g$  and  $T$  are the gas constant and temperature,  $\lambda_K = \gamma V_m / (R_g T)$  is the Kelvin length,  $\gamma$  is the surface tension of the liquid,  $V_m$  is the molar volume of the liquid,  $D$  is the diffusion constant of the vapor molecules in the surrounding air,  $M_w$  is the molar mass,  $P$  is the actual vapor pressure, and  $P_0$  is the saturation vapor pressure. Thus,  $P/P_0$  is the relative vapor pressure or, in our case, the relative humidity. For water at 25 °C, the parameters are  $\rho = 997 \text{ kg m}^{-3}$ ,  $\gamma = 0.072 \text{ N m}^{-1}$ ,  $V_m = 18.1 \times 10^{-6} \text{ m}^3$ ,  $M_w = 18.02 \text{ g mol}^{-1}$ ,  $\lambda_K = 0.526 \text{ nm}$ , and  $P_0 = 3169 \text{ Pa}$ . The diffusion coefficient of water in air at ambient pressure is  $D = 2.6 \times 10^{-5} \text{ m}^2 \text{ s}^{-1}$ . If we choose a typical tip radius of  $R = 30 \text{ nm}$  and a relative humidity of  $P/P_0 = 0.1$ , we get  $\tau = 0.11 \mu\text{s}$ . For  $P/P_0 = 0.9$ , the characteristic condensation/evaporation time increases to  $\tau = 0.28 \mu\text{s}$ . Since the minimal contact time in all experiments was  $\sim 75 \mu\text{s}$ , capillary bridges had sufficient time to form.

### Conclusions

For the interaction between silicon nitride with crystalline  $\text{CH}_3$ -terminated SAMs, two regimes can be distinguished. At loading rates below  $10^4$ – $10^5 \text{ nN s}^{-1}$ , the adhesion force increased proportional to the logarithm of the loading rate. The adhesion is most likely dominated by van der Waals attraction. At higher loading rates, the adhesion force was again proportional to the logarithm of the loading rate. The increase was, however, significantly steeper. The existence of this second regime is related to

the presence of the thiol monolayer and its specific end group. We could not clarify the underlying molecular mechanism governing the separation process at such high loading rates.

On OH-terminated SAMs, the adhesion force was  $\sim 6$  times higher than that on the  $\text{CH}_3$ -terminated SAMs, even at low humidity. This can partially be explained by hydrogen bonds forming between the hydroxyl groups of the monolayer and silanol groups of the tip. At a humidity above 10%, the capillary force further increased the adhesion force. The adhesion force increased to reach a maximum between 40% and 80% relative humidity depending on the specific experiment. The increase is most likely due to surface roughness of the tip, since it influences the meniscus formation. The decrease after the maximum is caused by a decreasing capillary force due to the small tip size. Adhesion force versus loading rate ( $F_{\text{ad}}$  versus  $r_F$ ) curves increased roughly linearly over the whole range of loading rates. The slope depended on the humidity, and it is correlated with the absolute strength of the capillary force.

An important result of the experiments was to identify two questions, which cannot yet be answered: Why are adhesion forces on noncrystalline  $\text{CH}_3$ -terminated SAM so much stronger than those on crystalline ones? What causes the strong adhesion on OH-terminated SAMs?

**Acknowledgment.** H.G. thanks the European Union for the fellowship of Marie Curie Actions “Analytical Methods in the Development of Science and Technology of Polymers” (ADMIST) and the fellowship of Max Planck Society for the International Max Planck Research School for Polymer Materials Science (IMPRS-PMS).